Supplementary Materials

Mechanical Anisotropy in Two-Dimensional Selenium Atomic Layers

Jing-Kai Qin[1,4,5†], Chao Sui[1,2†], Zhao Qin[6], Jianyang Wu[7], Hua Guo[2], Liang Zhen[4], Cheng-Yan Xu[4], Yang Chai[8], Chao Wang[1,2*], Xiaodong He[1,3*], Peide D Ye[5*] and Jun Lou[2*]

[1]*Center for Composite Materials and Structures, Harbin Institute of Technology, Harbin 150080, China*

[2]*Department of Materials Science and NanoEngineering, Rice University, Houston, TX 77005, USA*

[3]*Shenzhen STRONG Advanced Materials Research Institute Co., Ltd, PR China*

[4]*Sauvage Laboratory for Smart Materials, School of Materials Science and Engineering, Harbin Institute of Technology (Shenzhen), Shenzhen, 518055, China*

[5]*School of Electrical and Computer Engineering, Purdue University, West Lafayette, IN 47907, USA*

[6]*Department of Civil and Environmental Engineering, Syracuse University, Syracuse, NY 13244, USA*

[7]*Department of Physics, Research Institute for Biomimetics and Soft Matter, Fujian Provincial Key Laboratory for Soft Functional Materials Research, Xiamen University, Xiamen 361005, China*

[8]*Department of Applied Physics, The Hong Kong Polytechnic University, Hong Kong, China*

*Address correspondence to: chaowang@hit.edu.cn (C.W), hexd@hit.edu.cn (X.D.H), yep@purdue.edu (P.D.Y), jlou@rice.edu (J.L)

[†]These authors contributed equally.

This file includes:

Section S1. Preparation and morphology characterizations of 2D *t*-Se NSs.

Section S2. Sample preparation for Raman testing.

Section S3. Raman characterization for anisotropic structure of 2D *t*-Se NSs.

Section S4. Raman responses of 2D *t*-Se NSs under tensile and compression strains.

Section S5. *In-situ* SEM tensile testing for *t*-Se NSs.

Section S6. MD simulation.

Section S7. DFT calculation.

Table S1. Geometry and mechanical properties of *t*-Se NSs.

Figure S1. The PVD growth of ultrathin *t*-Se NSs.

Figure S2. Morphology characterizations and effective thickness measurement of *t*-Se NSs.

Figure S3. Raman characterization for *t*-Se NSs.

Figure S4. The angle-dependent Raman spectrum of *t*-Se NSs in the polar representation.

Figure S5. Raman spectra of PMMA spin-coated *h*-BN/*t*-Se/*h*-BN sandwich structure on PET substrate after 100 times of bending, where the tensile strain is 0.87%.

Figure S6. Schematic of setup of Raman testing for *t*-Se NS under strains along *c*-axis and *a/b*-axis.

Figure S7. The evolution of Raman spectra of *t*-Se NSs as applied with compressive strain.

Figure S8. TEM characterization of *t*-Se NSs at the fractured surface.

Other Supplementary Materials for this manuscript include the following:

Movie S1. *In-situ* tension of a *t*-Se NS (*c*-#1) along *c*-axis.

Movie S2. *In-situ* tension of a *t*-Se NS (*a/b*-#3) along *a/b*-axis.

Movie S3. Tensile video of a *t*-Se NS along *c*-axis based on MD simulation.

Movie S4. Tensile video of a *t*-Se NS along *a/b*-axis based on MD simulation.

Section S1. Preparation and morphology characterizations of 2D *t*-Se NSs

The growth process of *t*-Se NSs were shown in Figure S1a. High purity Se power (Sigma-Aldrich, 99.99%) was placed at the center of small quartz tube (diameter of 8 mm) with double side openings, and the Si (111) substrate was first etched by buffered oxide etching (BOE) solution to remove SiO_2 layer, and then cleaned by distilled water. Si substrates were placed at the end of quartz tube where the temperature is maintained at 100 °C. Finally, the small quartz tube was inserted into the heating center of a larger tube. During growth, the tube was kept under vacuum with a pressure less than 10 mbar. The whole reaction was carried out at the temperature of 210 °C for 60 min. After growth, the Si (111) substrate was coated with a layer of polycrystalline *t*-Se films. Some 2D *t*-Se NSs protruded out of the film surface and showed a typical oriented growth mode. The ribbon-like morphology of *t*-Se NSs were shown in Figure S1b. The atomic force microscopy (AFM) was used to determine the thickness of the samples (Figure S2). It was found that the NSs exhibit a variety of color contrast dependent on the thickness in the optical microscopy (OM) images. With the increase of the thickness, the color contrast changes from the blue to the gold. Additionally, when the thickness is more than 65 nm, clear strips can be observed due to its in-plane assembly of parallel ultra-narrow nanowires.

Section S2. Sample preparation for Raman testing

We found that the *t*-Se NS is very sensitive to the laser irradiation, and the bare *t*-Se NS on PET substrate can be easily damaged by Raman laser irradiation after only one-time measurement, leaving a burned hole on the *t*-Se NS surface (Figure S3a). To

resolve this issue, monolayer *h*-BN film was introduced to protect the sample by fabricating a *h*-BN/*t*-Se/*h*-BN sandwich structure (Figure S3b-c). After coving the *h*-BN film, the Raman peaks of *t*-Se NSs showed much less degradation even after ten-time measurements under same condition (Figure S3d). Additionally, it was found that the intensity of the Raman peaks in this sandwich structure could be enhanced by 5 times than that of bare *t*-Se.

Section S3. Raman characterization for anisotropic structure of 2D *t*-Se NSs

In order to reveal the anisotropic structure of 2D *t*-Se NSs, the PET substrate with *h*-BN/*t*-Se/*h*-BN sandwich structure was mounted onto a rotation stage which could be tuned from 0° to 360° during measurement, so that the Raman response of *t*-Se NS along different directions can be detected. The *t*-Se NS was first placed with *c*-axis parallel to the incident photon polarization, and the angle θ in this configuration is defined as 0°.

For our material system, the frequency peak at 233 cm^{-1} is labeled as E_2 mode, and it involves the asymmetric stretching of atoms along quasi-1D chains. The peak at 237 cm^{-1} (A_1) is originated from the chain expansion where Se atoms moves along in-plane direction.[1] The intensity of a given Raman mode is related to the Raman tensor and scattering geometry, and it is proportional to the expression equation:[2]

$$I = |e_i \times R \times e_s|^2 \qquad (S1)$$

where e_i is the unit vector of incident laser polarization and e_s stands for the scattering phonon polarization. R is the Raman tensor for a certain vibration mode. Here we assign the angle between incident laser polarization and *c*-axis of the lattice of

t-Se to be θ. According to the generalized form of Raman tensors, the intensity of E_2 and A_1 Raman modes are closely related to θ, which reach the local maxima when e_s is parallel along the direction of lattice vibration. For the asymmetric stretching mode of E_2, its Raman vector is three dimensional. However, the Raman vector for the A_1 mode is two-dimensional.[3-5] They can be written as:

$$R_{E_2} = \begin{pmatrix} A & & \\ & B & \\ & & C \end{pmatrix} \tag{S2}$$

$$R_{A_1} = \begin{pmatrix} & E \\ E & \end{pmatrix} \tag{S3}$$

in our experimental setup, e_i is parallel to e_s, and they can be written as $e_i = e_s{}^T = (\cos\theta, \theta, \sin\theta)$. Back substituting into Eq. (S1), we have

$$I_{E_2} = (A\cos^2\theta + C\sin^2\theta)^2 \tag{S4}$$

$$I_{A_1} = E^2 \sin^2 2\theta \tag{S5}$$

Figure S4 shows normalized Raman intensity in the polar representation and theoretical fitting curve according to above derivation. It can be seen that the theoretical calculation is in good agreement with the experimental data. Meanwhile, the E_2 mode has four branches, with the maxima and minima at 41° and 356°, respectively. However, the mode A_1 yields a 2-lobed shape, and the maximum intensity can be obtained at an angle of ~84°. This angle happens to be parallel to *a/b*-axis direction where Se atoms are connected by weak vdW interaction between atomic chains.

Section S4. Raman responses of 2D *t*-Se NSs under tensile and compression strains

In this study, we employed a four-point bending system to measure the Raman signals of *t*-Se NSs under tensile and compressive strains. The as-grown *t*-Se NS with irregular trapezium shape was first transferred onto one layer of *h*-BN on PET substrate

with the assistance of scotch tape. Then, another layer of h-BN was covered on the t-Se NS, by which the h-BN/t-Se/h-BN sandwich structure on PET substrate can be obtained. To ensure that the tensile strain can be effectively transferred to the t-Se NSs and corresponding strain-dependent Raman signal can be collected, one layer of PMMA (thickness 200 nm) was spin-coated on top of the h-BN/t-Se/ h-BN sandwich structure. As shown in Figure S5, the integrity of t-Se NS can be well reserved, and the Raman peaks do not show any shift and are barely degenerated even after 100 times of bending, demonstrating the feasibility of our experimental setup. As discussed in the main text, the t-Se NS crystallizes with the straight edge along the c-axis direction. Therefore, we can easily identify the crystal orientation of t-Se NS through direct observation in optical microscopy. As shown in Figure S6, we first place the PET substrate with the straight edge of t-Se NS parallel with bending direction, by which the strain originated from bending effect can be applied along c-axis of t-Se NS. Then, it is easy to rotate the PET substrate by 90° for the Raman measurement along a/b-axis.

Based on above experimental setup and Raman testing, the Raman responses of t-Se NS under tensile and compressive strains can be obtained. In this study, to keep the consistence with the tensile fracture behaviors of t-Se NSs, we mainly discuss the change of vibrational properties under tensile strain in the main text. And the Raman responses along c-axis and a/b-axis under compression strains are shown in Figure S7. One can see that both E_2 and A_1 modes would shift towards the higher position with compression strain applied along the c-axis direction, with the shift rate of 1.15 cm^{-1}%$^{-1}$ for E_2 mode and 0.7 cm^{-1}%$^{-1}$ for A_1 mode, respectively. Similar to the case of tensile

strained *t*-Se NS, the frequency position also fluctuates with no tendency, as the compression strain is applied on *t*-Se NS along *a/b*-axis.

Section S5. *In-situ* SEM tensile testing for *t*-Se NSs

The *in-situ* nanomechanical testing was performed inside the chamber of a SEM (FEI Quanta 400), where the individual *t*-Se NSs loaded on the microfabricated device were stretched by an Agilent In-SEM nanoindenter based on the established "push-pull" mechanism.[6, 7] It was noted that, in our previous work, we found that the interfacial bonding based on vdW interaction between 2D nanomaterials and smooth shuttle becomes dominant for the 2D nanomaterials with nano-scale thickness, and can serve as clamp to fix the samples.[6, 7, 8] To ensure that the interfacial adhesion force between *t*-Se NS and Si shuttles can sustain the tensile loading until the sample completely fracture, the contact area between *t*-Se NS and Si shuttles needs be adequately large. The tensile loading versus time curves can be directly obtained. Combining with the corresponding *in-situ* tensile movie, the force versus displacement curves can be extracted. In this study, totally sixteen samples were tested, where eleven samples are loaded along *c*-axis and five samples are loaded along *a/b*-axis. The geometrical parameters and measured mechanical properties of *t*-Se NSs were summarized in Table S1. Meanwhile, in order to reveal the fracture mechanisms of *t*-Se NSs, the fracture surfaces of samples were observed in HRTEM as shown in Figure S8.

Section S6. MD simulation

MD calculation was performed using the Large-scale Atomic/Molecular Massively Parallel Simulator (LAMMPS) program. We included the modified

Stillinger-Weber potential to the LAMMPS code to compute the energy and atomic

force of Se atoms,[9] where the energy is given by

$$U = \sum_{i<j} V_2(r_{ij}) + \sum_{i<j<k} V_3(r_{ij})V_3(r_{ik})\left[m_1(\cos(\theta) - \cos(\theta_0))^2 + m_3 - 0.5m_1\cos^4(\theta)\right] \qquad (S6)$$

where m_1=34.4866, m_3=11.9572 and θ_0=95.3688° are constants fitted for Se. The first

part is for the 2-body interaction, and the second part is for the 3-body interaction. By

taking the derivative of this many-body potential we compute the atomic forces and use

them to update the atomic coordinates during the MD simulation. We use a canonical

ensemble (NVT) by keeping the number of particles, the system volume and

temperature (at 10 k, to avoid structural fluctuation) to be constant during the simulation.

The time step is selected to be 1 fs that yield a stable simulation. We model the single

layer of t-Se with the size 170×170 nm^2, which include ~500,000 atoms according to

the t-Se crystal structure measured in experiment, and relax the structure by energy

minimization and equilibration for 100 ps. We deformed the material by using a

constant strain rate (0.0001/ps) applied in different directions of the nanosheet and

record the deformation as well as the stress-strain response during the deformation.

Visual Molecular Dynamics (VMD) is used to visualize the simulation result after the

simulation runs.

Section S7. DFT calculation

DFT calculation was performed using the Vienna ab initio simulation package

(VASP) program. The electron interactions of the studied Se system are described by

the projector-augmented waves (PAW) potentials. The exchange correlation energy

functional was evaluated by using the generalized-gradient approximation parameterized by Perdew, Burke, and Ernzerhof (GGA-PBE). The valence electrons were computed by the plane-wave basis set with an energy cutoff of 650 eV. The long-range dispersive interactions between neighboring Se chains are described by the vdW density functional (vdW-DF). The solutions are considered self-consistent as the difference in energies of two subsequent steps is less than 10^{-5} eV. Monkhorst-Pack k-point sets of $1\times1\times4$ are sampled for the Se cell system. All Se atoms in the calculation cell are optimized using the internal VASP procedure until all atomic forces are lower than 10 meV/Å.

References

[S1] Qin, J. K.; Qiu, G.; Jian, J.; Zhou, H.; Yang, L. M.; Charnas, A.; Zemlyanov, D. Y.; Xu, C. Y.; Xu, X. F.; Wu, W. Z.; Wang, H. Y.; Ye, P. D. D., Controlled Growth of a Large-Size 2D Selenium Nanosheet and Its Electronic and optoelectronic Applications. *Acs Nano* **2017,** *11* (10), 10222-10229.

[S2] Qiu, G.; Du, Y.; Charnas, A.; Zhou, H.; Jin, S.; Luo, Z.; Zemlyanov, D. Y.; Xu, X.; Cheng, G. J.; Ye, P. D., Observation of Optical and Electrical In-Plane Anisotropy in High-Mobility Few-Layer $ZrTe_5$. *Nano Letters* **2016,** *16*, 7364-7369.

[S3] Geick R.; Schröder U.; Stuke J., Lattice Vibrational Properties of Trigonal Selenium. physica status solidi (b) **1967,** *24*(1), 99-108.

[S4] Wang Y.X.; Qiu G.; Wang R.X.; Huang S.Y.; Wang Q.X.; Liu Y.Y.; Du Y.C.; Goddard W.A.; Kim M.J.; Xu X.F.; Ye P.D.; Wu W.Z., Field-effect transistors made from solution-grown two-dimensional tellurene. Nature Electronics, **2018,** *1*(4): 228-236.

[S5] Du, Y.; Qiu, G.; Wang, Y.; Si, M.; Xu, X.; Wu, W.; Ye, P. D., One-Dimensional van der Waals Material Tellurium: Raman Spectroscopy under Strain and Magneto-Transport. *Nano Letters* **2017,** *17*, 3965-3973.

[S6] Zhang, P.; Ma, L.; Fan, F.; Zeng, Z.; Peng, C.; Loya, P. E.; Liu, Z.; Gong, Y.; Zhang, J.; Zhang, X.; Ajayan, P.M.; Zhu, T.; Lou, J., Fracture toughness of graphene. *Nature Communications* **2014,** *5*, 3782.

[S7] Yang, Y.; Li, X.; Wen, M.; Hacopian, E.; Chen, W.; Gong, Y.; Zhang, J.; Li, B.; Zhou, W.; Ajayan, P. M.; Chen Q.; Zhu, T.; Lou, J., Brittle Fracture of 2D $MoSe_2$.

Advanced Materials **2016,** *29* (2), 1604201.1-1604201.7.

[S8] Fang, Q.; Sui, C.; Wang, C.; Zhai, T.; Zhang, J.; Liang, J.; Guo, H.; Sandoz-Rosado, E.; Lou, J., Strong and flaw-insensitive two-dimensional covalent organic frameworks. *Matter* **2021,** *4*, 1-12.

[S9] Oligschleger, C.; Jones, R. O.; Reimann, S. M.; Schober, H. R., Model interatomic potential for simulations in selenium. *Physical Review B* **1996,** *53* (10), 6165-6173.

Table S1. Geometry and mechanical properties of *t*-Se NSs.

Sample	Initial length (μm)	Width (μm)	Thickness (nm)	Fracture strain (%)	Young's modulus (GPa)	Fracture strength (GPa)
c-#1	6.29	5.67	15	0.92	25.32	0.33
c-#2	3.27	9.53	32	2.39	15.57	0.28
c-#3	3.18	14.86	32	1.33	16.22	0.13
c-#4	3.10	3.54	15	1.20	36.00	0.42
c-#5	6.23	4.77	39	2.73	38.24	0.63
c-#6	3.40	7.56	15	1.13	35.81	0.77
c-#7	6.31	10.47	15	1.63	15.46	0.30
c-#8	5.58	5.29	17	3.55	43.24	0.82
c-#9	3.39	5.52	45	2.36	8.59	0.11
c-#10	6.68	3.85	20	0.85	31.34	0.56
c-#11	3.41	4.96	36	0.80	12.73	0.15
a/b-#1	6.24	10.24	22	1.58	2.88	0.063
a/b-#2	3.34	8.24	28	1.77	4.50	0.094
a/b-#3	6.32	13.51	32	3.39	1.63	0.052
a/b-#4	3.59	11.28	25	4.18	1.95	0.045
a/b-#5	3.15	12.83	41	4.92	3.32	0.056
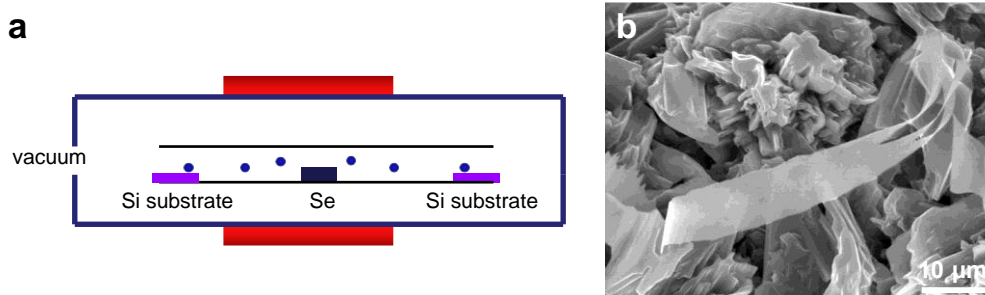
Figure S1. The PVD growth of ultrathin *t*-Se NSs. (a) Schematic illustration for the growth of *t*-Se

NSs. (b) SEM image of *t*-Se NSs as-grown on Si (111) substrate.
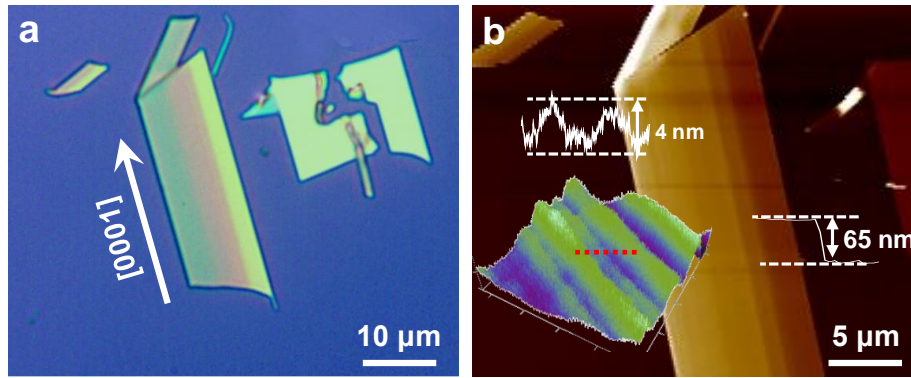
Figure S2. Morphology characterizations and effective thickness measurement of *t*-Se NSs. (a)

Optical microscopy image for 65 nm-thick *t*-Se NS. (b) Corresponding AFM height profile. Inset
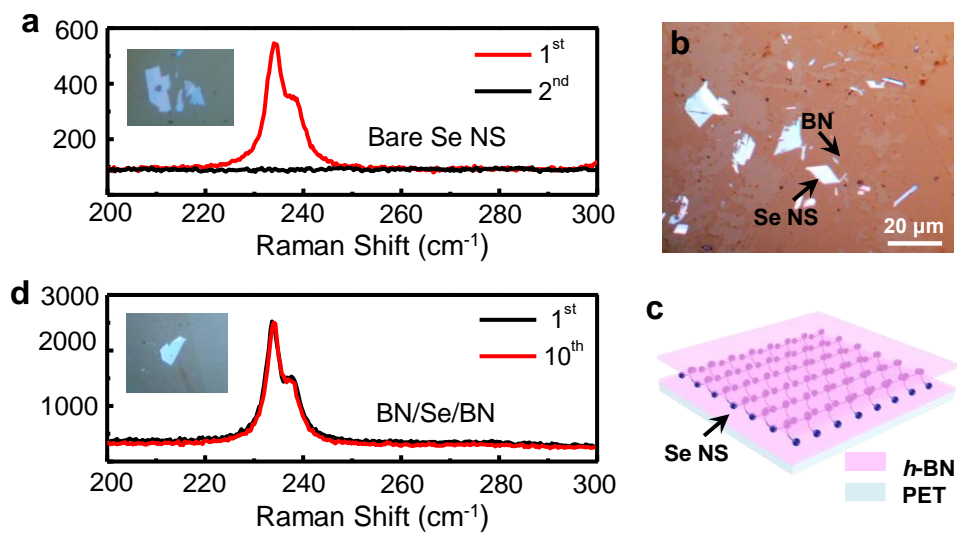
image shows the enlarged 3D-view image.

Figure S3. Raman characterization for *t*-Se NSs. (a) Raman spectrum of bare *t*-Se NS on PET substrate, the inset image shows a burned hole on the *t*-Se NS after one-time measurement. (b) Optical image for the *t*-Se NS covered by a monolayer *h*-BN film. (c) A schematic for the *h*-BN/*t*-Se/*h*-BN sandwich structure. (d) Raman spectrum of *h*-BN/*t*-Se/*h*-BN sandwich structure after one-time and ten-time measurements with the same illumination power intensity.
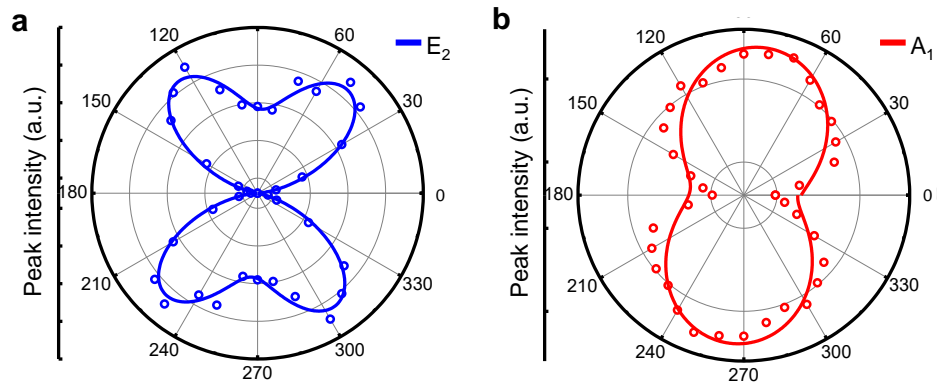
Figure S4. The angle-dependent Raman spectrum of *t*-Se NSs in the polar representation. (a-b)

The normalized intensity of E_2 and A_1 Raman modes in the polar representation.
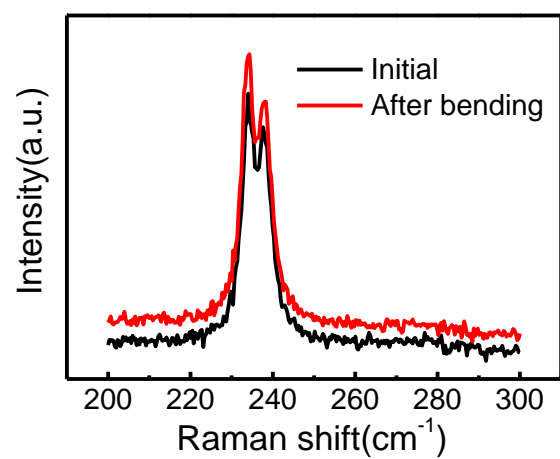
Figure S5. Raman spectra of PMMA spin-coated *h*-BN/*t*-Se/*h*-BN sandwich structure on PET

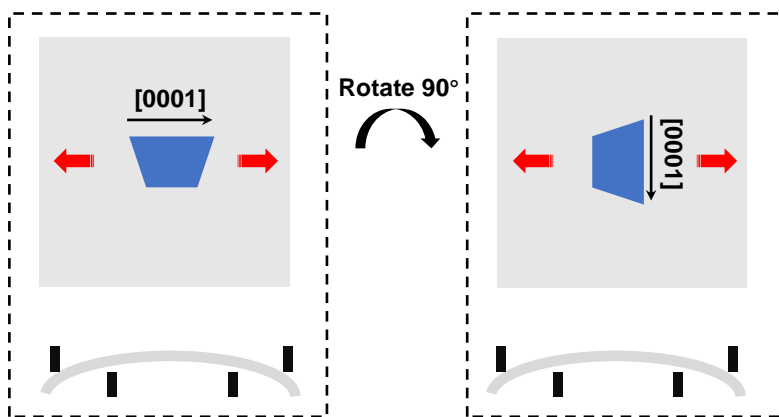substrate after 100 times of bending, where the tensile strain is 0.87%.

Figure S6. Schematic of setup of Raman testing for *t*-Se NS under strains along *c*-axis and *a/b*-
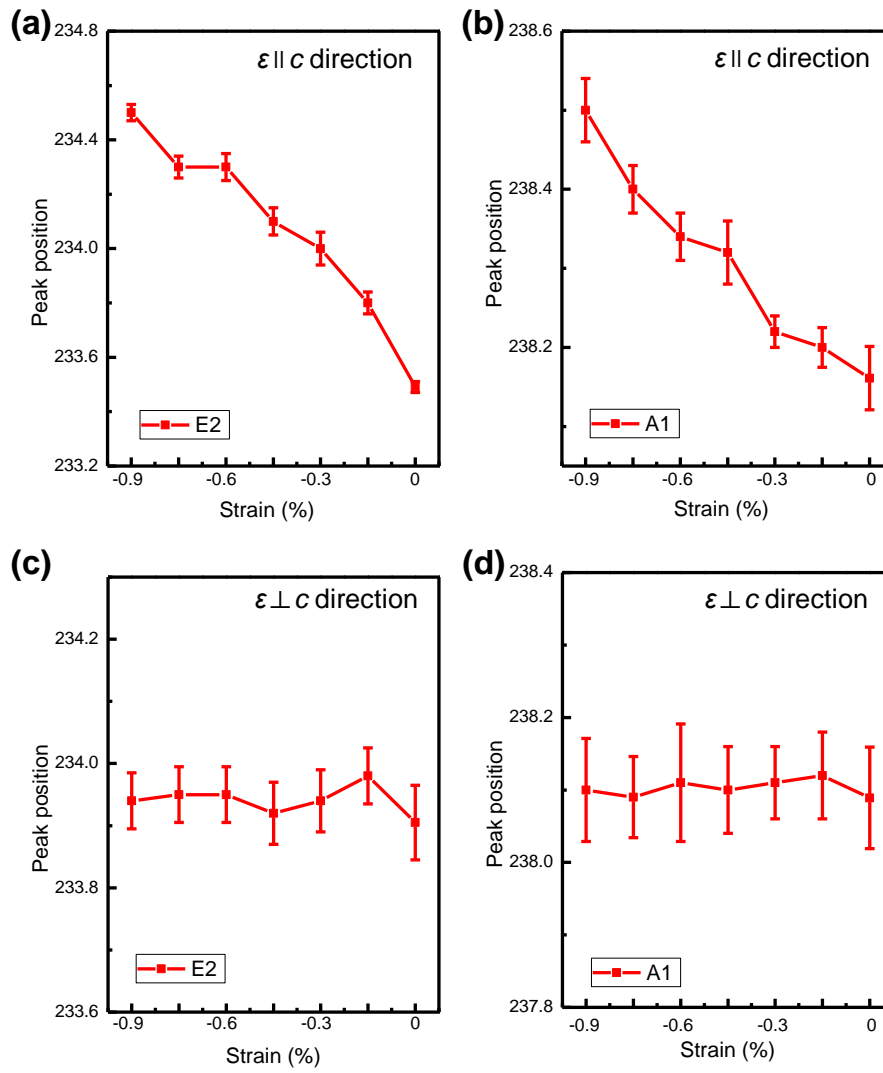
axis.

Figure S7. The evolution of Raman spectra of *t*-Se NSs as applied with compressive strain. (a-b) Raman shifts of E_2 and A_1 modes as a function of compressive strain ε along *c*-axis. (c-d) Raman shifts of E_2 and A_1 modes as a function of compressive strain ε along *a/b*-axis.
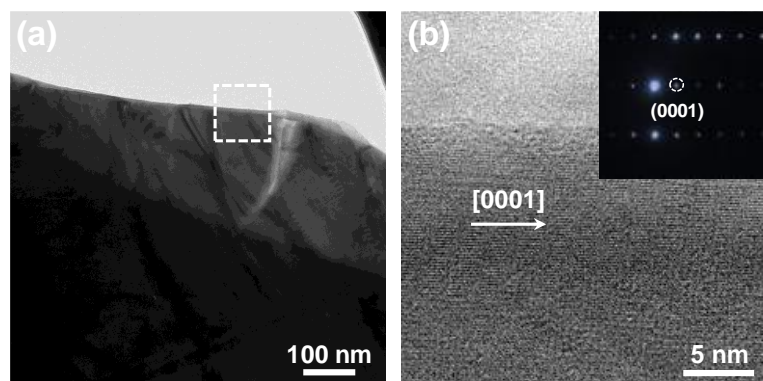
Figure S8. TEM characterization of *t*-Se NSs at the fractured surface. (a) Low-magnification TEM image for the crack edge of a fractured *t*-Se NS. (b) HRTEM image for the marked area in (a), where the inset image is corresponding SAED pattern.